

A Framework for Navigation with LTE Time-Correlated Pseudorange Errors in Multipath Environments

Kimia Shamaei¹, Joshua J. Morales¹, and Zaher M. Kassas^{1,2}

¹Department of Electrical Engineering and Computer Science, University of California, Irvine, USA

²Department of Mechanical and Aerospace Engineering, University of California, Irvine, USA

Emails: kshamaei@uci.edu, joshum9@uci.edu, zkassas@ieee.org

Abstract—A navigation framework based on a multi-state constraint Kalman filter (MSCKF) is proposed to reduce the effect of time-correlated pseudorange measurement noise of cellular long-term evolution (LTE) signals. The proposed MSCKF framework captures the position of the antenna over a window of measurements to impose constraints on the position estimate. Simulation results are presented showing a reduction of 57% and 51% in the two-dimensional (2D) and three-dimensional (3D) position root mean squared-error (RMSE), respectively, using the proposed framework compared to an extended Kalman filter (EKF). Experimental results on a ground vehicle navigating in an urban environment are presented showing a reduction of 29% and 64.7% in the 2D and 3D position RMSE, respectively, and a reduction of 19.6% and 86.7% in the 2D and 3D maximum error, respectively, using the proposed framework compared to an EKF.

I. INTRODUCTION

Cellular long-term evolution (LTE) signals have attracted significant attention for navigation as either a complement or an alternative to global navigation satellite system (GNSS), in GNSS-challenged environments [1]–[6]. LTE has several desirable characteristics for navigation including: abundance, high received power, geometric diversity, large transmission bandwidth, and free to use [7].

Received LTE signals experience more multipath compared to GNSS signals, particularly for ground-based receivers in urban canyons, due to the low elevation angles at which signals are received. LTE base stations (also known as evolved node Bs or eNodeBs) are stationary and the change in multipath depends on the receiver and environmental dynamics. In a low dynamic environment, the multipath effect lasts over multiple epochs and the error due to multipath is time-correlated. Several methods have been proposed to remove the effect of multipath, which are either at the signal processing level [8]–[10] or at the hardware level [11], [12]. The high transmission bandwidth of LTE signals (up to 20 MHz) is advantageous in resolving multipath effects [13]–[15].

In a Kalman filter, the measurement noise is assumed to be time-uncorrelated. A time-correlated measurement noise induces an error in estimating the navigation solution. Since the dynamics of the errors due to multipath is unknown at the receiver, whitening approaches cannot be used to decorrelate the measurement noise [16]. A multi-state constraint Kalman

filter (MSCKF) was originally proposed in the robotics literature for navigating in environments with *stationary* landmarks to impose geometric constraints on the pose state estimate [17]. In [18], the MSCKF was adapted to environments with dynamic stochastic states to deal with time-correlated measurement noise, where an inertial measurement unit (IMU) was used to capture the position of the LTE antenna over a sliding window of pseudorange measurements. The sliding window of measurement epochs along with the antenna motion helps decorrelate the measurement noise and provides constraints on the position estimate. Moreover, the difference between the clock bias of the receiver and each of the LTE eNodeBs were estimated along with the antenna’s position since the eNodeBs’ clock biases are unknown to the receiver. The performance of the MSCKF framework in [18] was evaluated for different sliding window lengths, showing reduction in the position root mean squared-error (RMSE) by increasing the length of the window. It was also shown that for large sliding window lengths, the payoff diminishes.

This paper extends [18] and makes two contributions. First, explicit details of the proposed navigation framework are provided, including state propagation and augmentation and model update. Second, simulation and experimental results are provided evaluating the effect of the correlation coefficient between two measurement epochs on the navigation solution error. Experimental results on a ground vehicle navigating in an urban environment show a reduction of 29% and 64.7% in the 2D and 3D position RMSE, respectively, and a reduction of 19.6% and 86.7% in the 2D and 3D maximum error, respectively, using the proposed framework compared to an extended Kalman filter (EKF).

The remainder of this paper is organized as follows. Section II discusses the proposed navigation framework structure. Section III presents simulation results. Section IV presents experimental results. Section V concludes the paper.

II. NAVIGATION FRAMEWORK

A. State Vector

The vehicle’s state vector \mathbf{x}_r is defined as

$$\mathbf{x}_r \triangleq [\mathbf{x}_{\text{IMU}}^T, \mathbf{x}_{\text{clk}}^T, \boldsymbol{\pi}_1^T, \boldsymbol{\pi}_2^T, \dots, \boldsymbol{\pi}_N^T]^T,$$

where \mathbf{x}_{IMU} represents the IMU state vector, \mathbf{x}_{clk} is the clock error state vector, and $\boldsymbol{\pi}_i$ is composed of the receiver's position and the difference between the clock bias of the receiver and each of the eNodeBs at the i -th pseudorange measurement.

The IMU state vector is given by

$$\mathbf{x}_{\text{IMU}} \triangleq \left[{}^I_G \bar{\mathbf{q}}^\top, {}^G \mathbf{r}_{\text{IMU}}^\top, {}^G \mathbf{v}_{\text{IMU}}^\top, \mathbf{b}_g^\top, \mathbf{b}_a^\top \right]^\top,$$

where ${}^I_G \bar{\mathbf{q}}$ is the unit quaternion representing the rotation from a global frame G , such as an Earth-centered inertial (ECI) frame, to the IMU frame I ; ${}^G \mathbf{r}_{\text{IMU}}$ and ${}^G \mathbf{v}_{\text{IMU}} = {}^G \dot{\mathbf{r}}_{\text{IMU}}$ are the 3D position and velocity of the IMU in the global frame, respectively; and \mathbf{b}_g and \mathbf{b}_a are the gyroscope and accelerometer biases, respectively.

The clock error state vector is defined as

$$\mathbf{x}_{\text{clk}} \triangleq \left[\mathbf{x}_{\text{clk}}^{(1)\top}, \dots, \mathbf{x}_{\text{clk}}^{(U)\top} \right]^\top,$$

where U is the total number of eNodeBs; $\mathbf{x}_{\text{clk}}^{(u)} = [c\Delta\delta t^{(u)}, c\Delta\dot{\delta}t^{(u)}]$; $\Delta\delta t^{(u)} = \delta t_r - \delta t_s^{(u)}$ with δt_r and $\delta t_s^{(u)}$ representing the clock biases of the receiver and the u -th eNodeB, respectively; $\Delta\dot{\delta}t^{(u)} = \dot{\delta}t_r - \dot{\delta}t_s^{(u)}$ with $\dot{\delta}t_r$ and $\dot{\delta}t_s^{(u)}$ representing the clock drifts of the receiver and the u -th eNodeB, respectively.

The vector $\boldsymbol{\pi}_i$ is defined as

$$\boldsymbol{\pi}_i \triangleq \left[{}^G \mathbf{r}_{A_i}^\top, \mathbf{x}_{\text{clk}, b_i}^\top \right]^\top,$$

where $\mathbf{x}_{\text{clk}, b_i} = [c\Delta\delta t_i^{(1)}, \dots, c\Delta\delta t_i^{(U)}]^\top$ is the difference between the clock bias of the receiver and each of the eNodeBs and ${}^G \mathbf{r}_{A_i}$ is the antenna's position in the global frame at the i -th pseudorange measurement epoch.

B. IMU State Propagation

The IMU produces measurements of the rotational velocity $\boldsymbol{\omega}_m$ and linear acceleration \mathbf{a}_m every T seconds, which are modeled as

$$\boldsymbol{\omega}_m(k) = {}^I \boldsymbol{\omega}(k) + \mathbf{b}_g(k) + \mathbf{n}_g(k), \quad (1)$$

$$\mathbf{a}_m(k) = C \left({}^I_G \bar{\mathbf{q}}(k) \right) \left({}^G \mathbf{a}(k) - {}^G \mathbf{g}(k) \right) + \mathbf{b}_a(k) + \mathbf{n}_a(k), \quad (2)$$

where ${}^I \boldsymbol{\omega}$ is the true rotational velocity of the IMU; \mathbf{n}_g and \mathbf{n}_a are the gyroscope and accelerometer measurement noises with zero-mean and covariances $\sigma_g^2 \mathbf{I}_{3 \times 3}$ and $\sigma_a^2 \mathbf{I}_{3 \times 3}$, respectively; $\mathbf{I}_{m \times m}$ is an $m \times m$ identity matrix; ${}^G \mathbf{a}$ is the 3D linear acceleration; ${}^G \mathbf{g}$ is the acceleration due to gravity; and $C \left({}^I_G \bar{\mathbf{q}} \right)$ is the equivalent rotation matrix of ${}^I_G \bar{\mathbf{q}}$.

The IMU measurements are used to propagate the IMU state estimate. The orientation estimate is propagated according to

$${}^I_{G^{k+1|j}} \hat{\mathbf{q}} = {}^I_{G^k} \hat{\mathbf{q}} \otimes {}^I_{G^k|j} \hat{\mathbf{q}}, \quad \text{for } k \geq j,$$

where \otimes is the quaternion multiplication operator and ${}^I_{G^k} \hat{\mathbf{q}}$ is the relative rotation of the IMU frame from time-step k to $k+1$, which is obtained using a fourth-order Runge-Kutta numerical solver [19].

The IMU position state estimate is propagated using trapezoidal integration according to

$${}^G \hat{\mathbf{r}}_{\text{IMU}}(k+1|j) = {}^G \hat{\mathbf{r}}_{\text{IMU}}(k|j) + \frac{T}{2} \left[{}^G \hat{\mathbf{v}}_{\text{IMU}}(k+1|j) + {}^G \hat{\mathbf{v}}_{\text{IMU}}(k|j) \right],$$

where ${}^G \hat{\mathbf{v}}_{\text{IMU}}(k+1|j)$ is the propagated IMU velocity state estimate, which is obtained using trapezoidal integration according to

$${}^G \hat{\mathbf{v}}_{\text{IMU}}(k+1|j) = {}^G \hat{\mathbf{v}}_{\text{IMU}}(k|j) + \frac{T}{2} \left[\hat{\mathbf{s}}(k) + \hat{\mathbf{s}}(k+1) \right] + T {}^G \mathbf{g},$$

where $\hat{\mathbf{s}}(k) = \mathbf{C}^\top \left({}^I_{G^k} \hat{\mathbf{q}} \right) \hat{\mathbf{a}}(k)$ and $\hat{\mathbf{a}} = \mathbf{a}_m - \hat{\mathbf{b}}_a$.

The gyroscope and accelerometer biases state estimates are propagated according to

$$\hat{\mathbf{b}}_g(k+1|j) = \hat{\mathbf{b}}_g(k|j), \hat{\mathbf{b}}_a(k+1|j) = \hat{\mathbf{b}}_a(k|j).$$

C. Clock State Propagation

The clock state estimate is propagated according to

$$\hat{\mathbf{x}}_{\text{clk}}(k+1|j) = \mathbf{F}_{\text{clk}} \hat{\mathbf{x}}_{\text{clk}}(k|j), \quad (3)$$

where $\mathbf{F}_{\text{clk}} = \text{diag} \left[\mathbf{F}_{\text{clk}}^{(1)}, \dots, \mathbf{F}_{\text{clk}}^{(U)} \right]$ and $\mathbf{F}_{\text{clk}}^{(u)} = \begin{bmatrix} 1 & T \\ 0 & 1 \end{bmatrix}$.

D. Covariance Propagation

The one-step prediction error covariance matrix of the IMU and clock states is given by

$$\mathbf{P}(k+1|j) = \mathbf{F}(k) \mathbf{P}(k|j) \mathbf{F}(k)^\top + \mathbf{Q}, \quad (4)$$

where $\mathbf{F} \triangleq \text{diag} [\mathbf{F}_{\text{IMU}}, \mathbf{F}_{\text{clk}}]$ and $\mathbf{Q} = \text{diag} [\mathbf{Q}_{\text{IMU}}, \mathbf{Q}_{\text{clk}}]$; \mathbf{F}_{IMU} is the linearized DT IMU state transition matrix and \mathbf{Q}_{IMU} is the linearized DT IMU state process noise covariance matrix. The detailed derivations of \mathbf{F}_{IMU} and \mathbf{Q}_{IMU} are described in [20], [21].

The clock process noise covariance matrix \mathbf{Q}_{clk} is given by

$$\mathbf{Q}_{\text{clk}} = \begin{bmatrix} \mathbf{Q}_{\text{clk}_1} & \mathbf{Q}_{\text{clk}_r} & \dots & \mathbf{Q}_{\text{clk}_r} \\ \mathbf{Q}_{\text{clk}_r} & \mathbf{Q}_{\text{clk}_2} & \dots & \mathbf{Q}_{\text{clk}_r} \\ \vdots & \vdots & \ddots & \vdots \\ \mathbf{Q}_{\text{clk}_r} & \mathbf{Q}_{\text{clk}_r} & \dots & \mathbf{Q}_{\text{clk}_U} \end{bmatrix},$$

where $\mathbf{Q}_{\text{clk}_r}$ and $\mathbf{Q}_{\text{clk}_u}$ are defined as

$$\mathbf{Q}_{\text{clk}_u} \triangleq \mathbf{Q}_{\text{clk}_r} + \mathbf{Q}_{\text{clk}_s}^{(u)},$$

$$\mathbf{Q}_{\text{clk}_r} = \begin{bmatrix} S_{\tilde{w}_{\delta t_r}} T + S_{\tilde{w}_{\delta t_r}} \frac{T^3}{3} & S_{\tilde{w}_{\delta t_r}} \frac{T^2}{2} \\ S_{\tilde{w}_{\delta t_r}} \frac{T^2}{2} & S_{\tilde{w}_{\delta t_r}} T \end{bmatrix},$$

where $S_{\tilde{w}_{\delta t_r}}$ and $S_{\tilde{w}_{\delta t_r}}$ are the clock bias and drift process noise power spectra, respectively. It has been shown through laboratory experiments that the power spectral density of the fractional frequency deviation $y(t)$ of an oscillator from its nominal frequency can be characterized according to $S_y(f) = \sum_{\alpha=-2}^2 h_\alpha f^\alpha$, where $\{h_\alpha\}_{\alpha=-2}^2$ are the power-law coefficients. A common approximation involves only the h_0 and h_{-2}

parameters, namely $S_{\tilde{w}_{\delta t_r}} \approx \frac{h_{0_r}}{2}$ and $S_{\tilde{w}_{\delta t_s}} \approx 2\pi^2 h_{-2_r}$ [22]. The structure of $\mathbf{Q}_{\text{clk}_s}^{(u)}$ is similar to $\mathbf{Q}_{\text{clk}_r}$, except that $S_{\tilde{w}_{\delta t_r}}$ and $S_{\tilde{w}_{\delta t_s}}$ are replaced with $S_{\tilde{w}_{\delta t_s}}^{(u)}$ and $S_{\tilde{w}_{\delta t_r}}^{(u)}$, respectively.

E. State Augmentation

The antenna position estimate is computed from the IMU pose estimate at every pseudorange measurement epoch according to

$${}^G\hat{\mathbf{r}}_A(k|j) = {}^G\hat{\mathbf{r}}_{\text{IMU}}(k|j) + \mathbf{C}^\top \begin{pmatrix} I_{k|j} \hat{\mathbf{q}} \\ \mathbf{G} \end{pmatrix} I \hat{\mathbf{r}}_A,$$

where $I \hat{\mathbf{r}}_A$ is the position of the antenna in the IMU frame and is known *a priori*. The antenna position and the difference between the clock bias of the receiver and each of the eNodeBs are augmented to the state vector. The covariance matrix of the state estimate is augmented according to

$$\mathbf{P}_{\text{AUG}}(k|j) \leftarrow \begin{bmatrix} \mathbf{I}_L \\ \mathbf{J} \end{bmatrix} \mathbf{P}_{\text{AUG}}(k|j) \begin{bmatrix} \mathbf{I}_L \\ \mathbf{J} \end{bmatrix}^\top,$$

where $L = 15 + 2U + (3+U)n$, $n = 0, \dots, N-1$ is the number of pseudorange measurements augmented to the measurement vector, $\mathbf{P}_{\text{AUG}}(k|j) \triangleq \mathbf{P}(k|j)$ for $n = 0$, and \mathbf{J} is the Jacobian matrix given by

$$\mathbf{J} = \begin{bmatrix} [\mathbf{C}_{\hat{\mathbf{q}}}^\top I \mathbf{r}_A \times] & \mathbf{I}_3 & \mathbf{0}_{3 \times 9} & \mathbf{0}_{3 \times 2U} & \mathbf{0}_{3 \times (3+U)n} \\ \mathbf{0}_{U \times 3} & \mathbf{0}_{U \times 3} & \mathbf{0}_{U \times 9} & \mathbf{K} & \mathbf{0}_{U \times (3+U)n} \end{bmatrix},$$

where $\mathbf{C}_{\hat{\mathbf{q}}}^\top \triangleq \mathbf{C}^\top \begin{pmatrix} I_{k|j} \hat{\mathbf{q}} \\ \mathbf{G} \end{pmatrix}$; $\mathbf{K} = [e_0, \dots, e_{U-1}]^\top$; e_i is a vector of length $2U$, where its $2i$ -th element is one and the rest are zeros; $\mathbf{0}_{m \times n}$ is an $m \times n$ matrix of zeros; and $[\boldsymbol{\omega} \times]$ is the skew-symmetric matrix of vector $\boldsymbol{\omega}$ defined as

$$[\boldsymbol{\omega} \times] \triangleq \begin{bmatrix} 0 & -\omega_z & \omega_y \\ \omega_z & 0 & -\omega_x \\ -\omega_y & \omega_x & 0 \end{bmatrix}, \quad \boldsymbol{\omega} = [\omega_x, \omega_y, \omega_z]^\top.$$

The augmented covariance matrix \mathbf{P}_{AUG} can be partitioned as

$$\mathbf{P}_{\text{AUG}}(k|j) = \begin{bmatrix} \mathbf{P}(k|j) & \mathbf{P}_c(k|j) \\ \mathbf{P}_c^\top(k|j) & \mathbf{P}_A(k|j) \end{bmatrix},$$

where \mathbf{P}_A is the covariance matrix of the estimate of (i) antenna's positions and (ii) difference between the clock biases of the receiver and each of the eNodeBs and \mathbf{P}_c is the cross correlation of the evolving IMU and clock states with the estimate of the antenna's positions and the difference between the clock biases. When an IMU measurement is available, the IMU and clock state estimates and the covariance matrix \mathbf{P} are propagated according to (4). The augmented covariance matrix is propagated according to

$$\mathbf{P}_{\text{AUG}}(k+1|j) = \begin{bmatrix} \mathbf{P}(k+1|j) & \mathbf{F}(k)\mathbf{P}_c(k|j) \\ \mathbf{P}_c^\top(k|j)\mathbf{F}^\top(k) & \mathbf{F}(k)\mathbf{P}_A(k|j)\mathbf{F}^\top(k) \end{bmatrix}.$$

F. Measurement Update

After $N+1$ pseudorange measurement epochs to all U eNodeBs, the vector $\boldsymbol{\rho}$ is formed as

$$\boldsymbol{\rho} = [\boldsymbol{\rho}^{(1)\top}, \dots, \boldsymbol{\rho}^{(U)\top}]^\top,$$

where $\boldsymbol{\rho}^{(u)} = [\rho^{(u)}(0), \dots, \rho^{(u)}(N)]^\top$ and

$$\rho^{(u)}(i) = \begin{cases} h^{(u)}({}^G\mathbf{r}_A(i)) + c\Delta\delta t^{(u)}(i) + v^{(u)}(i), & \text{if } i = 0, \dots, N-1, \\ h^{(u)}({}^G\mathbf{r}_{\text{IMU}} + \mathbf{C}_{\hat{\mathbf{q}}}^\top I \mathbf{r}_A) + c\Delta\delta t^{(u)}(i) + v^{(u)}(i), & \text{otherwise,} \end{cases}$$

where $h^{(u)}(\mathbf{r}) \triangleq \|\mathbf{r}_s^{(u)} - \mathbf{r}\|$, $\mathbf{r}_s^{(u)}$ is the position of the u -th eNodeB, and $v^{(u)}(i)$ is the measurement noise. Assuming the measurement noise to be independent for different eNodeBs, the measurement noise covariance matrix can be expressed as

$$\mathbf{R} = \text{diag}[\mathbf{R}^{(1)}, \dots, \mathbf{R}^{(U)}],$$

where the (i, j) -th element of $\mathbf{R}^{(u)}$ is defined as

$$\mathbf{R}^{(u)}(i, j) = \begin{cases} \sigma^{(u)2}(i), & \text{if } i = j \\ \varrho^{(u)}(i, j) \sigma^{(u)}(i) \sigma^{(u)}(j), & \text{otherwise.} \end{cases}$$

where $\sigma^{(u)}(i)$ is the standard deviation of $v^{(u)}(i)$ and $\varrho^{(u)}(i, j)$ is the correlation coefficient of the measurement noise between time step i and j . The residual can be modeled as

$$\mathbf{r} = \boldsymbol{\rho} - \hat{\boldsymbol{\rho}} = \mathbf{H}\tilde{\mathbf{x}} + \mathbf{v},$$

where \mathbf{H} is the Jacobian matrix defined as $\mathbf{H} = \begin{bmatrix} \mathbf{H}^{(1)} \\ \vdots \\ \mathbf{H}^{(U)} \end{bmatrix}$,

with the i -th row of $\mathbf{H}^{(u)}$ given by

$$\mathbf{H}^{(u)}(i) = \begin{cases} [\mathbf{0}_{1 \times (15+2U)} \quad \mathbf{0}_{1 \times (3+U)} \cdots \mathbf{A}^{(u)}(i) \cdots \mathbf{0}_{1 \times (3+U)}], & \text{if } i = 0, \dots, N-1, \\ [\mathbf{B}^{(u)}(i) \quad \mathbf{0}_{1 \times (3+U)} \cdots \mathbf{0}_{1 \times (3+U)}], & \text{if } i = N, \end{cases}$$

where

$$\mathbf{A}^{(u)}(i) = \begin{bmatrix} \frac{(\mathbf{r}_s^{(u)} - {}^G\hat{\mathbf{r}}_A(i))^\top}{\|\mathbf{r}_s^{(u)} - {}^G\hat{\mathbf{r}}_A(i)\|} & \underbrace{\mathbf{0} \cdots \mathbf{0}}_{u-1} & 1 & 0 & \cdots & 0 \end{bmatrix},$$

$$\mathbf{B}^{(u)}(i) = \begin{bmatrix} [\mathbf{C}_{\hat{\mathbf{q}}}^\top I \mathbf{r}_A \times] & \frac{(\mathbf{r}_s^{(u)} - {}^G\hat{\mathbf{r}}_{\text{IMU}})^\top}{\|\mathbf{r}_s^{(u)} - {}^G\hat{\mathbf{r}}_{\text{IMU}}\|} & \underbrace{\mathbf{0} \cdots \mathbf{0}}_{2(u-1)} & 1 & 0 & \cdots & 0 \end{bmatrix}.$$

When an IMU measurement is available (i.e., every T), it is used to propagate the IMU pose estimate. When a pseudorange measurement is available (i.e., every LTE frame $T_{\text{sub}} = 10$ ms), the antenna's position and the difference between the clock bias of the receiver and each of the eNodeBs are augmented to the state vector. Once $N+1$ pseudorange measurement epochs are appended the measurement vector, an EKF update is performed. After each update, the states corresponding to the antenna's position and the difference between the clock bias of the receiver and each of the eNodeBs corresponding to N_{rem} epochs are removed from the state

vector. The pseudorange measurements corresponding to these states are also removed from the measurement vector and the filter returns to the state propagation stage. Therefore, the update is performed every $N_{\text{rem}}T_{\text{sub}}$. By increasing N_{rem} , the time correlation between the measurement vectors of two consecutive updates decreases. However, increasing N_{rem} decreases the update rate. Therefore, the choice of N_{rem} depends on the level of time-correlation in the measurement noise and the application requirements for the update rate.

III. SIMULATION RESULTS

To evaluate the proposed framework, a simulation environment was developed for a receiver navigating in an urban area (downtown Riverside, California) over a 6 km trajectory that includes straight segments and turns. The locations of the eNodeBs were simulated using real eNodeBs' locations in that environment. The simulation environment showing the receiver's trajectory and the eNodeBs' positions is shown in Fig. 1.



Fig. 1. Simulated traversed trajectory and the positions of the LTE eNodeBs. Map data: Google Earth.

The receiver's and eNodeBs' clocks were simulated with a temperature-compensated crystal oscillator (TCXO) and an oven-controlled crystal oscillator (OCXO), respectively, where $h_{0_r} = 9.4 \times 10^{-20}$, $h_{-2_r} = 3.8 \times 10^{-21}$, $h_{0_s}^{(u)} = 8 \times 10^{-20}$ and $h_{-2_s}^{(u)} = 4 \times 10^{-23}$, where $u = 1, \dots, 6$.

The IMU's rotational velocity and linear acceleration measurements were generated at $T = 10$ ms according to equations (1) and (2), respectively. The IMU's measurement noise and time evolution of the IMU's biases set according to the grade of the IMU. In this work, data for a consumer-grade IMU was generated.

It was assumed that the LTE pseudoranges were estimated every LTE frame duration, which is $T_{\text{sub}} = 10$ ms. A Rayleigh and a Rician fading model can be used to model the propagation of the wireless channel. In a Rayleigh fading, it is assumed that the signal does not have line-of-sight (LOS), while in the Rician fading channel, it is assumed that the signal has LOS. In this section, the receiver is assumed to have access to LOS. Therefore, a Rician fading channel was used to model the channel impulse response (CIR). Moreover, to characterize the LOS and multipath signal power and delay profile, the CIR was simulated based on an extended vehicular A (EVA) channel model [23] and the multipath error

affecting the pseudorange was simulated based on the model presented in [24], [25]. The correlation coefficient between the measurements at two consecutive epochs was assumed to be constant, i.e., $\rho^{(u)}(i, j) = \rho$ over the entire simulation. The simulation was repeated for 20 different multipath and noise conditions.

Fig. 2 shows the average of the 2D and 3D position RMSE over the entire simulated trajectory for each run using the EKF framework and the proposed framework. The results are compared for different values of ρ and for $N = 50$ and $N_{\text{rem}} = N/2$. Solid lines show the results for MSCKF and dashed lines show the results for EKF. It can be seen that for correlated measurement noise, the proposed MSCKF framework has lower RMSE compared to the EKF framework. The reduction in 3D RMSE is more significant compared to the 2D RMSE.

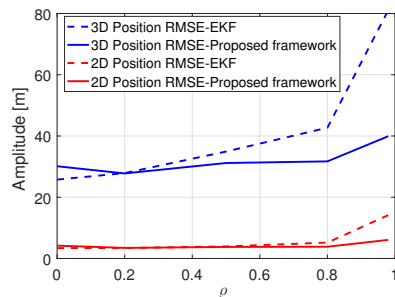


Fig. 2. EKF and proposed framework 2D and 3D position RMSE over the entire simulated trajectory for different correlation coefficients

IV. EXPERIMENTAL RESULTS

To evaluate the performance of the proposed framework, an experiment was performed in an urban area (downtown Riverside, California). In this experiment, a ground vehicle was equipped with two consumer-grade 800/1900 MHz cellular omnidirectional Laird antennas to receive LTE signals at 739 MHz and 1955 MHz carrier frequencies from the U.S. cellular provider AT&T. A dual-channel National Instruments (NI) universal software radio peripheral (USRP)-2954R, driven by a GPS-disciplined oscillator (GPSDO) was used to simultaneously down-mix and synchronously sample LTE signals with 10 Msps. A laptop was used to store LTE samples for post-processing. A Septentrio AsteRx-i V, which is equipped with dual antenna multi-frequency GNSS receiver with real-time kinematic (RTK) and a Vectornav VN-100 micro-electromechanical systems (MEMS) IMU, was used to estimate the position and orientation of the ground vehicle, which was used as the ground truth. Fig. 3 shows the experimental hardware setup.

The receiver traversed a trajectory of 1380 m over 190 s while listening to 5 eNodeBs. The stored LTE samples were processed by the Multichannel Adaptive Transceiver Information eXtractor (MATRIX) software-defined radio (SDR) developed by the Autonomous Systems Perception, Intelligence, and Navigation (ASPIN) Laboratory, producing pseudoranges



Fig. 3. Experimental hardware setup

to LTE eNodeBs in the environment [25]. The subaccumulation period was set to two LTE frames, which is $T_{\text{sub}} = 20$ ms.

The derived pseudoranges were used to estimate the receiver's position using the proposed MSCKF framework and the EKF framework. The receiver was assumed to have access to GPS signals at its initial position. Therefore, the receiver was able to estimate the initial values of its position and the difference of its clock bias with each of the eNodeBs, which makes the problem observable [26], [27]. The AsteRx-i V's GNSS-INS provides orientation, position, velocity, and their covariances, which were used to initialize both the MSCKF and EKF frameworks. The gyroscope's and accelerometer's biases and their measurement noise covariances were initialized by taking the mean and variance of 5 seconds of stationary IMU data, respectively. The receiver and eNodeBs clocks were modeled as OCXO with $h_{0_r} = 8 \times 10^{-20}$, $h_{-2_r} = 4 \times 10^{-23}$, $h_{0_s}^{(u)} = 2.6 \times 10^{-22}$, and $h_{-2_s}^{(u)} = 4 \times 10^{-26}$, where $u = 1, \dots, 5$. The initial values of the difference of the clock bias and drift of the receiver with each of the eNodeBs were set to 1 m and 0.01 m/s with initial covariance of 1 m^2 and $0.01 \text{ m}^2/\text{s}^2$, respectively. The measurement noise variance was determined empirically.

Fig. 4(a) shows the 2D and 3D position RMSE and maximum error for different values of N . In these results, it is assumed that $\rho = 0.99$ and $N_{\text{rem}} = \lfloor N/2 \rfloor$. It can be seen that 2D and 3D position RMSE and maximum error are decreased by increasing N . The payoff due to increasing N from 50 to 100 diminishes. Fig. 4(b) shows the 2D and 3D position RMSE for different values of ρ . In these results, $N = 50$ and $N_{\text{rem}} = \lfloor N/2 \rfloor$. It can be seen that higher ρ decreases the position RMSE, which shows that the pseudorange measurements' errors were highly correlated. The results show that the proposed framework could reduce the 2D and 3D position RMSE by 29% and 64.7%, respectively, and the 2D and 3D maximum error by 19.6% and 86.7%, respectively, compared with the EKF approach.

Fig. 5 shows the navigation solution errors in east-north-up (ENU) frame and their corresponding $\pm 3\sigma$ bounds for the EKF and proposed frameworks. It can be seen that the navigation solution error is lower for the proposed framework compared to an EKF. It can also be seen that the error in the proposed framework is within the estimated covariance bounds, which means that the filter is consistent. This is not the case for the results obtained by an EKF framework. Note that the growing vehicle's vertical estimation uncertainty is due to a lack of

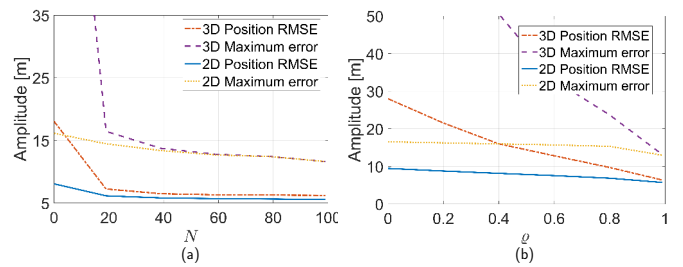


Fig. 4. Experimental 2D and 3D position RMSE for (a) different numbers of states to augment and (b) different values of correlation coefficient

TABLE I
2D AND 3D POSITION RMSE

Method	2D RMSE [m]	3D RMSE [m]	2D Max. error [m]	3D Max. error [m]
EKF	8.06	18.04	16.13	98.90
Proposed framework	5.72	6.37	12.97	13.15

both vehicle's vertical motion and eNodeB's vertical geometric diversity. A calibrated altimeter would help reduce the vertical error and uncertainty.

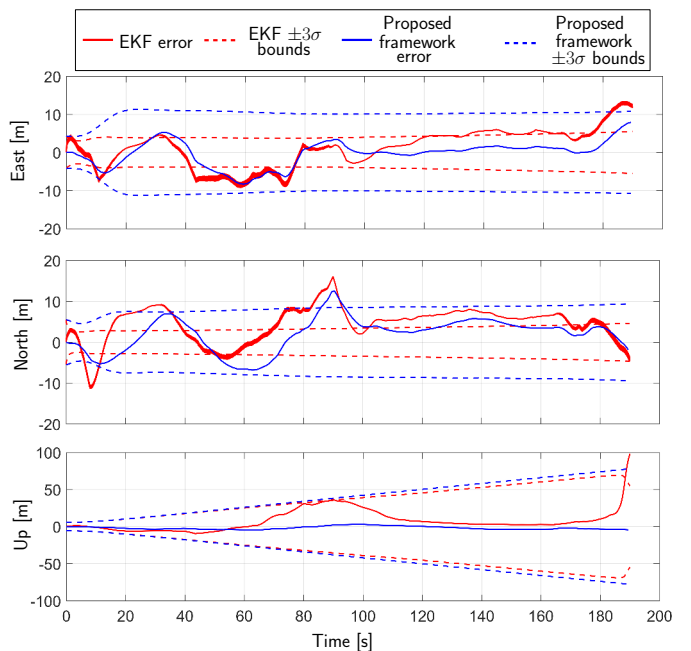


Fig. 5. Navigation solution errors in ENU frame and their corresponding estimated $\pm 3\sigma$ bounds for the EKF and proposed framework

Fig. 6 compares the navigation solutions obtained by the proposed MSCKF framework and the EKF framework versus the ground truth. Table I summarizes the resulting 2D and 3D position RMSE and maximum error.

V. CONCLUSION

This paper considered reducing the effect of induced errors in the EKF due to time-correlated pseudorange LTE errors. A framework based on an MSCKF was proposed to reduce



Fig. 6. Experimental results showing the vehicle's ground truth trajectory (from a GNSS-IMU RTK system) and the estimated trajectory with the proposed MSCKF framework and an EKF. The total traversed trajectory was 1380 m. Image: Google Earth

the positioning error by maintaining a sliding window of the receiver's position and clock biases in a state vector and imposing probabilistic constraints between these states. The proposed framework's states propagation, augmentation, and update were described in details. Then, simulation results were presented to compare the performance of the proposed approach with the EKF for different correlation coefficients. Experimental results showed a reduction of 29% and 64.7% in the 2D and 3D position RMSE, respectively, and a reduction of 19.6% and 86.7% in the 2D and 3D maximum error, respectively, using the proposed framework compared to an EKF.

ACKNOWLEDGMENT

This work was supported in part by the Office of Naval Research (ONR) under Grant N00014-16-1-2305.

REFERENCES

- [1] C. Gentner, E. Munoz, M. Khider, E. Staudinger, S. Sand, and A. Dammann, "Particle filter based positioning with 3GPP-LTE in indoor environments," in *Proceedings of IEEE/ION Position, Location and Navigation Symposium*, April 2012, pp. 301–308.
- [2] F. Knutti, M. Sabathy, M. Driusso, H. Mathis, and C. Marshall, "Positioning using LTE signals," in *Proceedings of Navigation Conference in Europe*, April 2015, pp. 1–8.
- [3] M. Driusso, C. Marshall, M. Sabathy, F. Knutti, H. Mathis, and F. Babich, "Vehicular position tracking using LTE signals," *IEEE Transactions on Vehicular Technology*, vol. 66, no. 4, pp. 3376–3391, April 2017.
- [4] K. Shamaei, J. Khalife, and Z. Kassas, "Exploiting LTE signals for navigation: Theory to implementation," *IEEE Transactions on Wireless Communications*, vol. 17, no. 4, pp. 2173–2189, April 2018.
- [5] K. Shamaei, J. Khalife, and Z. Kassas, "Ranging precision analysis of LTE signals," in *Proceedings of European Signal Processing Conference*, August 2017, pp. 2788–2792.
- [6] K. Shamaei, J. Khalife, and Z. Kassas, "Pseudorange and multipath analysis of positioning with LTE secondary synchronization signals," in *Proceedings of Wireless Communications and Networking Conference*, 2018, pp. 286–291.
- [7] Z. Kassas, J. Khalife, K. Shamaei, and J. Morales, "I hear, therefore I know where I am: Compensating for GNSS limitations with cellular signals," *IEEE Signal Processing Magazine*, pp. 111–124, September 2017.
- [8] R. van Nee, "The multipath estimating delay lock loop," in *Proceedings of Spread Spectrum Techniques and Applications Symposium*, November 1992, pp. 39–42.
- [9] M. Psiaki, T. Ertan, B. O'Hanlon, and S. Powell, "GNSS multipath mitigation using antenna motion," *NAVIGATION, Journal of the Institute of Navigation*, vol. 62, no. 1, pp. 1–22, Spring 2015.
- [10] K. Pesyna, T. Humphreys, R. Heath, T. Novlan, and J. Zhang, "Exploiting antenna motion for faster initialization of centimeter-accurate GNSS positioning with low-cost antennas," *IEEE Transactions on Aerospace and Electronic Systems*, vol. 53, no. 4, pp. 1597–1613, August 2017.
- [11] T. Pany, N. Falk, B. Riedl, C. Stober, J. Winkel, and H. Ranner, "GNSS synthetic aperture processing with artificial antenna motion," in *Proceedings of ION GNSS Conference*, September 2013, pp. 3163–3171.
- [12] M. Yaqoob, F. Tufvesson, A. Mannesson, and B. Bernhardsson, "Direction of arrival estimation with arbitrary virtual antenna arrays using low cost inertial measurement units," in *Proceedings of International Conference on Communications Workshops*, June 2013, pp. 79–83.
- [13] J. del Peral-Rosado, J. Lopez-Salcedo, G. Seco-Granados, F. Zanier, and M. Crisci, "Achievable localization accuracy of the positioning reference signal of 3GPP LTE," in *Proceedings of International Conference on Localization and GNSS*, June 2012, pp. 1–6.
- [14] W. Xu, M. Huang, C. Zhu, and A. Dammann, "Maximum likelihood TOA and OTDOA estimation with first arriving path detection for 3GPP LTE system," *Transactions on Emerging Telecommunications Technologies*, vol. 27, no. 3, pp. 339–356, 2016.
- [15] K. Shamaei, J. Khalife, and Z. Kassas, "Comparative results for positioning with secondary synchronization signal versus cell specific reference signal in LTE systems," in *Proceedings of ION International Technical Meeting Conference*, January 2017, pp. 1256–1268.
- [16] Y. Bar-Shalom, X. Li, and T. Kirubarajan, *Estimation with Applications to Tracking and Navigation*. New York, NY: John Wiley & Sons, 2002.
- [17] A. Mourikis and S. Roumeliotis, "A multi-state constraint Kalman filter for vision-aided inertial navigation," in *Proceedings IEEE International Conference on Robotics and Automation*, April 2007, pp. 3565–3572.
- [18] K. Shamaei, J. Morales, and Z. Kassas, "Positioning performance of LTE signals in Rician fading environments exploiting antenna motion," in *Proceedings of ION GNSS Conference*, September 2018, pp. 3423–3432.
- [19] J. Morales, P. Roysdon, and Z. Kassas, "Signals of opportunity aided inertial navigation," in *Proceedings of ION GNSS Conference*, September 2016, pp. 1492–1501.
- [20] J. Farrell and M. Barth, *The Global Positioning System and Inertial Navigation*. New York, NY: McGraw-Hill, 1998.
- [21] P. Groves, *Principles of GNSS, Inertial, and Multisensor Integrated Navigation Systems*, 2nd ed. Artech House, 2013.
- [22] A. Thompson, J. Moran, and G. Swenson, *Interferometry and Synthesis in Radio Astronomy*, 2nd ed. John Wiley & Sons, 2001.
- [23] 3GPP, "Evolved universal terrestrial radio access (E-UTRA); user equipment (UE) radio transmission and reception," 3rd Generation Partnership Project (3GPP), TS 136.101, June 2011. [Online]. Available: <http://www.3gpp.org/ftp/Specs/html-info/36212.htm>
- [24] B. Yang, K. Letaief, R. Cheng, and Z. Cao, "Timing recovery for OFDM transmission," *IEEE Journal on Selected Areas in Communications*, vol. 18, no. 11, pp. 2278–2291, November 2000.
- [25] K. Shamaei and Z. Kassas, "LTE receiver design and multipath analysis for navigation in urban environments," *NAVIGATION, Journal of the Institute of Navigation*, vol. 65, no. 4, pp. 655–675, December 2018.
- [26] Z. Kassas and T. Humphreys, "Observability analysis of collaborative opportunistic navigation with pseudorange measurements," *IEEE Transactions on Intelligent Transportation Systems*, vol. 15, no. 1, pp. 260–273, February 2014.
- [27] J. Morales and Z. Kassas, "Stochastic observability and uncertainty characterization in simultaneous receiver and transmitter localization," *IEEE Transactions on Aerospace and Electronic Systems*, 2018, accepted.